



# Systematic energy band gap control of pyrene based donor-acceptor-donor molecules for efficient chemosensor

So-Yeon Kim, Min-Ji Kim, Mina Ahn, Kyeong-Min Lee, Kyung-Ryang Wee\*

Department of Chemistry and Institute of Natural Science, Daegu University, Gyeongsan, 38453, Republic of Korea

## ARTICLE INFO

### Keywords:

Pyrene  
Substituents  
Intramolecular charge transfer  
Lippert-mataga plot  
Chemosensor  
Stern-volmer equation

## ABSTRACT

We have successfully prepared a series of pyrene based donor-acceptor-donor (D-A-D) molecules, 1,6-bis[(*N,N*-*p*-(*R*)-diphenylamino)phenyl]pyrene (*R* = CN (**Py-CN**), F (**Py-F**), H (**Py-H**), Me (**Py-Me**), and OMe (**Py-OMe**)), containing *N,N*-bis(*p*-(*R*)-phenyl)aniline as an electron donor and pyrene as an electron acceptor by using the Suzuki-Miyaura cross-coupling reaction in good yield and fully characterized. By introducing various *N,N*-bis(*p*-(*R*)-phenyl)aniline derivatives with electron-donating or electron-withdrawing *R* groups, the energy band gaps of **Py-R** were systematically controlled and emission colors were efficiently tuned from blue to yellow (441–536 nm). Absorption spectra of all **Py-R** compounds showed intramolecular charge transfer (ICT) transitions in the range of 350–450 nm in the ground state. Solvent-dependent emission spectra confirmed the substituent dependence of charge transfer ability in the excited state. Then, the charge transfer tendencies by the substituents were quantitatively observed using the Lippert-Mataga equation. The HOMO and LUMO energy levels of synthesized **Py-R** compounds were found in the range of –5.44 to –5.97 eV and –2.68 to –2.97 eV respectively from cyclic voltammetry (CV) experimental. Theoretical studies were conducted using density functional theory (DFT) and time-dependent DFT (TD-DFT) calculations to provide a basis for interpreting experimental data. Experimental and calculated values were found to be well correlated with the Hammett constants ( $\sigma_{para}$ ) and confirmed that the energy band gap was systematically controlled by the substituent effect. Furthermore, pyrene based D-A-D compounds with controllable band gap were employed as selective chemosensors to detect nitro explosives, and especially **Py-CN** demonstrated efficient sensing ability for *ortho*-nitroaniline (*o*-NA) by fluorescence quenching strategy.

## 1. Introduction

Systematic electronic state control and efficient energy band gap tuning are fundamental issues for molecular based optoelectronics or energy conversion devices such as organic light-emitting devices (OLEDs) [1–3], organic field-effect transistors (OFETs) [4,5], light-harvesting arrays [6], and organic photovoltaic cells (OPVs) [7,8]. In particular, polycyclic aromatic hydrocarbon (PAH) based donor-acceptor (D-A) systems are one of the efficient energy gap tunable material and play an important role in emerging technologies to achieve multi-functional optoelectronic properties, because effectively regulate the electronic structure by building blocks (ex. donor and/or acceptor unit) substitution at the active PAH sites [9,10]. Several research groups are trying to develop PAH based energy band gap tunable D-A materials that possess intramolecular charge transfer (ICT) properties [11–14]. For example, polyacene derivatives such as perylene [9,15], anthracene

[16], phenanthrene [17], and tetracene [18] have been used as emitting materials to produce efficient and stable emission for full-color OLEDs or organic light-emitting field-effect transistors (OLEFETs) with good chromaticities, luminescence efficiencies, and high device stabilities.

In particular, pyrene containing polyaromatic D-A compounds have received much attention among the various PAH based D-A materials, because they allow effective control of absorption and emission properties via regioselective functional group substitution of active pyrene sites at the 1, 3, 6, and 8-positions, as well as the K-regions at the 4, 5, 9, and 10-positions [19]. In addition, pyrene based D-A compounds are used as efficient light-emitting materials with high emission quantum yields in solution and solid states, and their color-tunable emission characteristics are usually originated ICT caused by donor or acceptor units. As previously reported, emission color tuning of pyrene based chromophores is readily controlled by functional group modification [10,20]. The planar nature of pyrene moiety geometry leads to

\* Corresponding author.

E-mail address: [krwee@daegu.ac.kr](mailto:krwee@daegu.ac.kr) (K.-R. Wee).

<https://doi.org/10.1016/j.dyepig.2021.109362>

Received 13 January 2021; Received in revised form 10 March 2021; Accepted 29 March 2021

Available online 4 April 2021

0143-7208/© 2021 Elsevier Ltd. All rights reserved.

intermolecular  $\pi$ - $\pi$  interactions and induces aggregation [19,21], fluorescence quenching [22], red-shift characteristics [23], and broad emission bands [10,20]. Among these properties, molecular aggregation and fluorescence quenching have been utilized by many studies seeking to develop fluorescence sensors [24,25].

To control energy band gap and provide effective emission color tuning in the pyrene based D-A compounds, the strengths of donor and/or acceptor containing the  $\pi$ -conjugated linker should be systematically modulated and the amount of charge transferred from donor to acceptor controlled. This can be achieved by (i) adjusting the configuration of D-A systems based on considerations of their molecular symmetries and asymmetries, for example, D-A-D and A-D-A types [10,20,26] and D-A and D- $\pi$ -A types [9,27,28], respectively, or by (ii) introducing an electron-donating or withdrawing group, which allows charge transfer properties to be adjusted within molecules containing a donor, acceptor, and  $\pi$ -linker [9,29]. Although color-tunable pyrene based D-A materials have been reported, knowledge of wide-range color control with broad energy band gap tuning by donor or acceptor substitutions on the symmetrical pyrene based molecule is lacking [9,10]. Therefore, we investigated systematic and wide energy band gap control with focus on their optical ICT properties using symmetrical D-A-D type compounds by connecting two-donor units grafted with various substituents on a pyrene core. Furthermore, these properties of pyrene based D-A-D compounds are pragmatic and useful in the fluorescence chemosensor research area.

The selective recognition and sensing of aromatic compounds is an important aspect of fluorescence recognition and is primarily driven by the fluorescence resonance energy transfer (FRET) mechanism [30,31]. In this context, compounds exhibiting ICT are mainly used for material sensing and selective energy transfer is controlled by emission or energy band gap tailoring. In particular, in chemosensor research, the detection of nitro aromatic explosive materials such as 2,4-dinitrotoluene (DNT) and 2,4,6-trinitrotoluene (TNT) is viewed as an important issue, because these nitro aromatic species have substantial adverse environmental effects due to their toxicities and environmental resistances, and hence, efficient methods of detecting these pollutants are urgently required [32–34]. Fluorescence method, one of the methods for detecting aromatic compounds, is widely used because of its sensitivity and sensing speed [30]. Wide range fluorescence emission molecules are attractive materials for chemosensor applications based on fluorescence quenching method. These molecules can be used as selective chemosensors to detect the analytes contain nitro aromatics, which are emission quenchers of chromophores through various quenching pathway.

In this study, we designed and synthesized a series of pyrene based D-A-D compounds (**Py-R**) consisting of two triphenylamine (TPA) donor units linked directly to pyrene at the 1,6- positions as an acceptor unit. Donor units were placed at the active sites on the pyrene core to achieve potent ICT effects. By introducing various TPA derivatives (*N,N*-bis(*p*-*R*)-phenyl)aniline) with electron-donating and withdrawing substituents, the energy band gaps of the D-A-D compounds were systematically controlled and emission colors were efficiently tuned from blue to yellow. Furthermore, ICT character was found to depend on the electron push-pull effects of substituents, which exhibited a gradual increase in ICT properties as electron-donating characteristics increased. To investigate structure-property relationships, the photophysical and electrochemical properties of **Py-R** were systematically demonstrated and compared with density functional theory (DFT) calculations. Finally, **Py-R** compounds are applied as fluorescence chemosensor using the energy band gap control characteristic, and in particular, we observed fluorescence quenching by *o*-NA for detect nitro aromatic explosive materials.

## 2. Experimental section

### 2.1. General conditions

Based on the standard Schlenk techniques, all of the synthesis experimental procedures were performed under a dry argon condition. Reagents and solvents were purchased from commercial sources and used as received without further purification, unless otherwise stated. All reactions were monitored with thin layer chromatography (TLC) using commercial TLC plates (Merck Co.). Silica gel column chromatography was carried out on silica gel 60 G (230–400 mesh ASTM, Merck Co.). The synthesized compounds were characterized by  $^1\text{H}$  NMR or  $^{13}\text{C}$   $\{^1\text{H}\}$ -NMR and elemental analysis at the Core Research Center for Natural Products and Medical Materials (CRCNM) in the Yeungnam University. The  $^1\text{H}$  and proton-decoupled  $^{13}\text{C}$  spectra were recorded on a Bruker500 spectrometer operating at 500 and 125 MHz, respectively, and all proton and carbon chemical shifts were measured relative to internal residual chloroform (99.5%  $\text{CDCl}_3$ ) from the lock solvent. The elemental analyses (C, H, N, O) were performed using a Thermo Fisher Scientific Flash 2000 series analyzer. The GC-MS analysis was performed using a highly sensitive gas chromatograph/mass selective detector spectrometer (Agilent, 7890B–5977B GC/MSD) at the Daegu Center of Korea Basic Science Institute. The 1,6-bis(4,4,5,5-tetramethyl-1,3,2-dioxaborolan-2-yl)pyrene (Py-B(pin)), 4-bromo-*N,N*-bis(4-cyanophenyl)aniline (TPA-CN), 4-bromo-*N,N*-bis(4-fluorophenyl)aniline (TPA-F), 4-bromo-*N,N*-diphenylaniline (TPA-H), 4-bromo-*N,N*-bis(4-methylphenyl)aniline (TPA-Me), and 4-bromo-*N,N*-bis(4-methoxyphenyl)aniline (TPA-OMe) were prepared on the basis of the previously published method [35,36]. The UV–vis absorption spectra were recorded with photodiode array spectrophotometry by Sinco Mega-2100, and the fluorescence emission measurements were carried out using Shimadzu fluorometer (RF-6000) with a wavelength resolution of  $\sim 1$  nm. Fluorescence lifetimes were measured by PicoQuant FluoTime 200 that takes advantage of the time-correlated single photon counting method. A pulsed diode laser operated at a 20 MHz repetition rate was used as the excitation source. The full width at half maximum (FWHM) of a laser pulse was typically 45 ps, and the instrument response function was  $\sim 190$  ps when the Hamamatsu photomultiplier tube (H5783-01) was used. The emission quantum yields ( $\Phi_{\text{PL}}$ ) were calculated using William's comparative method for samples of five different concentrations of (1–10)  $\mu\text{M}$ , using 9,10-diphenylanthracene ( $\Phi_{\text{PL}} = 0.95$ , ethanol) as a reference standard [37]. A CH Instruments 701D potentiostat was used for electrochemical measurements, and cyclic voltammetry (CV) was performed in an electrolytic solution prepared using 100  $\mu\text{M}$  electroactive compounds and 0.1 M tetrabutylammonium perchlorate ( $\text{Bu}_4\text{N-ClO}_4$ ) at RT under an argon atmosphere. A three-electrode configuration, glassy carbon, platinum wire, and SCE were used as working, counter, and reference electrodes, respectively.

### 2.2. Synthesis

#### 2.2.1. 1,6-bis[(*N,N*-*p*-*R*)-diphenylamino]phenyl]pyrene (**Py-R**)

A mixture of 1,6-bis(4,4,5,5-tetramethyl-1,3,2-dioxaborolan-2-yl)pyrene (Py-B(pin)) (0.30 g, 0.67 mmol), 4-bromo-*N,N*-bis(*p*-*R*)-phenyl)aniline (TPA-R) (1.03 g, 2.76 mmol, R = CN (TPA-CN), F (TPA-F), H (TPA-H), Me (TPA-Me), and OMe (TPA-OMe)),  $\text{K}_2\text{CO}_3$  (0.95 g, 6.89 mmol), and tetrakis(triphenylphosphine)palladium(0) (0.0069 g, 5 mol %) in 1,4-dioxane/ $\text{H}_2\text{O}$  (4:1, 30 mL) was refluxed under argon at 100  $^\circ\text{C}$  for overnight. After cooling to room temperature, deionized water (50 mL) was added and the organic layer was separated using a separating funnel. The water layer was washed using dichloromethane (DCM) ( $\times 3$ ) for extracted remained organic residue. After combined all of organic solvents, the organic layer was dried over anhydrous  $\text{MgSO}_4$ , and then filtered off. The residue was purified by silica gel column chromatography using DCM/*n*-hexane mixtures as eluents.

**Py-CN**. Brown powder (eluent DCM/*n*-hexane = 2:1). Yield: 71%

(0.37 g). Mp 238 °C.  $^1\text{H}$  NMR (500 MHz,  $\text{CDCl}_3$ , ppm):  $\delta$  8.19 (d,  $J = 7.5$  Hz, 2H), 8.17 (d,  $J = 9.0$  Hz, 2H), 8.03 (d,  $J = 9.0$  Hz, 2H), 7.95 (d,  $J = 8.0$  Hz, 2H), 7.60 (d,  $J = 8.0$  Hz, 4H), 7.55 (d,  $J = 9.0$  Hz, 8H), 7.26 (d,  $J = 8.5$  Hz, 4H), 7.19 (d,  $J = 9.0$  Hz, 8H).  $^{13}\text{C}\{^1\text{H}\}$  (125 MHz,  $\text{CDCl}_3$ , ppm):  $\delta$  150.2, 144.2, 141.0, 139.2, 136.6, 134.5, 134.4, 133.7, 132.4, 130.7, 127.7, 126.5, 124.8, 123.2, 118.8, 106.2. GC-MS Calculated for  $\text{C}_{56}\text{H}_{32}\text{N}_6$   $[\text{M}]^+$ : 788.27 g/mol, Found  $[\text{M}]^+$ : 788.3 g/mol. Anal. Calculated for  $\text{C}_{56}\text{H}_{32}\text{N}_6$ : C, 85.29; H, 4.13; N, 10.62. Found: C, 85.19; H, 4.23; N, 10.62.

**Py-F.** Greenish yellow powder (eluent DCM/*n*-hexane = 1:3). Yield: 78% (0.39 g). Mp 295 °C.  $^1\text{H}$  NMR (500 MHz,  $\text{CDCl}_3$ , ppm):  $\delta$  8.26 (d,  $J = 9.0$  Hz, 2H), 8.18 (d,  $J = 7.5$  Hz, 2H), 8.04 (d,  $J = 9.0$  Hz, 2H), 7.98 (d,  $J = 8.0$  Hz, 2H), 7.50 (d,  $J = 9.0$  Hz, 4H), 7.20–7.19 (m, 4H), 7.18–7.16 (m, 8H), 7.04 (t,  $J = 9.0$  Hz, 8H).  $^{13}\text{C}\{^1\text{H}\}$  (125 MHz,  $\text{CDCl}_3$ , ppm):  $\delta$  160.0, 158.0, 147.2, 143.8, 131.4, 130.2, 128.8, 127.7, 127.3, 126.3, 125.3, 125.2, 124.4, 122.0, 116.1. GC-MS Calculated for  $\text{C}_{52}\text{H}_{32}\text{F}_4\text{N}_2$   $[\text{M}]^+$ : 760.25 g/mol, Found  $[\text{M}]^+$ : 760.3 g/mol. Anal. Calculated for  $\text{C}_{52}\text{H}_{32}\text{F}_4\text{N}_2$ : C, 82.09; H, 4.24; N, 3.68. Found: C, 82.19; H, 4.14; N, 3.78.

**Py-H.** Greenish yellow powder (eluent DCM/*n*-hexane = 1:3). Yield: 75% (0.35 g). Mp 286 °C.  $^1\text{H}$  NMR (500 MHz,  $\text{CDCl}_3$ , ppm):  $\delta$  8.38 (d,  $J = 9.5$  Hz, 2H), 8.33 (d,  $J = 8.0$  Hz, 2H), 8.01 (d,  $J = 8.0$  Hz, 2H), 7.87 (d,  $J = 9.0$  Hz, 2H), 7.54 (d,  $J = 8.5$  Hz, 4H), 7.33 (t,  $J = 8.5$  Hz, 8H), 7.28 (d,  $J = 9.0$  Hz, 4H), 7.26–7.25 (m, 8H), 7.08 (t,  $J = 7.0$  Hz, 4H).  $^{13}\text{C}\{^1\text{H}\}$  (125 MHz,  $\text{CDCl}_3$ , ppm):  $\delta$  147.8, 147.1, 137.8, 136.4, 135.1, 131.4, 129.3, 127.9, 127.6, 127.4, 124.8, 124.6, 124.3, 123.3, 123.1. GC-MS Calculated for  $\text{C}_{52}\text{H}_{36}\text{N}_2$   $[\text{M}]^+$ : 688.29 g/mol, Found  $[\text{M}]^+$ : 688.5 g/mol. Anal. Calculated for  $\text{C}_{52}\text{H}_{36}\text{N}_2$ : C, 90.65; H, 5.24; N, 4.12. Found: C, 90.55; H, 5.34; N, 4.12.

**Py-Me.** Greenish yellow powder (eluent DCM/*n*-hexane = 1:2). Yield: 85% (0.37 g). Mp 293 °C.  $^1\text{H}$  NMR (500 MHz,  $\text{CDCl}_3$ , ppm):  $\delta$  8.28 (d,  $J = 9.5$  Hz, 2H), 8.17 (d,  $J = 8.0$  Hz, 2H), 8.03 (d,  $J = 9.0$  Hz, 2H), 7.98 (d,  $J = 7.5$  Hz, 2H), 7.47 (d,  $J = 8.5$  Hz, 4H), 7.19 (d,  $J = 9.0$  Hz, 4H), 7.13 (d,  $J = 9.0$  Hz, 16H), 2.35 (s, 12H).  $^{13}\text{C}\{^1\text{H}\}$  (125 MHz,  $\text{CDCl}_3$ , ppm):  $\delta$  147.4, 145.3, 137.6, 134.1, 132.7, 131.2, 130.2, 129.9, 128.8, 127.7, 127.2, 125.4, 124.9, 124.4, 122.0, 20.8. GC-MS Calculated for  $\text{C}_{56}\text{H}_{44}\text{N}_2$   $[\text{M}]^+$ : 744.35 g/mol, Found  $[\text{M}]^+$ : 744.4 g/mol. Anal. Calculated for  $\text{C}_{56}\text{H}_{44}\text{N}_2$ : C, 90.27; H, 5.97; N, 3.79. Found: C, 90.22; H, 5.92; N, 3.89.

**Py-OMe.** Bright yellow powder (eluent DCM/*n*-hexane = 1:1). Yield: 88% (0.48 g). Mp 228 °C.  $^1\text{H}$  NMR (500 MHz,  $\text{CDCl}_3$ , ppm):  $\delta$  8.28 (d,  $J = 9.0$  Hz, 2H), 8.16 (d,  $J = 8.0$  Hz, 2H), 8.02 (d,  $J = 9.5$  Hz, 2H), 7.97 (d,  $J = 8.0$  Hz, 2H), 7.44 (d,  $J = 9.0$  Hz, 4H), 7.19 (d,  $J = 9.0$  Hz, 8H), 7.10 (d,  $J = 8.5$  Hz, 4H), 6.88 (d,  $J = 9.0$  Hz, 8H), 3.82 (s, 12H).  $^{13}\text{C}\{^1\text{H}\}$  (125 MHz,  $\text{CDCl}_3$ , ppm):  $\delta$  155.9, 147.9, 140.9, 137.5, 131.1, 130.1, 128.8, 127.2, 126.7, 125.4, 124.3, 120.0, 114.78, 114.75, 114.72, 55.5. GC-MS Calculated for  $\text{C}_{56}\text{H}_{44}\text{N}_2\text{O}_4$   $[\text{M}]^+$ : 808.33 g/mol, Found  $[\text{M}]^+$ : 808.4 g/mol. Anal. Calculated for  $\text{C}_{56}\text{H}_{44}\text{N}_2\text{O}_4$ : C, 83.16; H, 5.45; N, 3.49; O, 7.94. Found: C, 83.06; H, 5.55; N, 3.44; O, 7.89.

### 2.3. Density functional theory calculations

Density functional theory (DFT) calculations were performed using the Gaussian'16 software package. Full geometry optimizations in their ground state were performed using the B3LYP functional and the 6-31G (d,p) basis set for all atoms. The excitation energies and oscillator strengths for the lowest 100 singlet–singlet transitions at the optimized geometry in the ground state were obtained in time-dependent DFT (TD-DFT) calculations using the same basis set and functional as for the ground state. All Isodensity plots of the frontier orbitals were visualized by Chem3D Ultra and GaussView softwares. More detail DFT/TD-DFT calculation results for **Py-R** were described in Supplementary data.

### 2.4. Chemosensor

The UV–vis absorption spectra were measured at 10  $\mu\text{M}$

concentrations for both the target analyte *o*-NA and **Py-R** compounds using Sinco Mega-2100 and the fluorescence emission measurements were performed by gradually increasing *o*-NA concentration ( $2.0 \times 10^{-4}$  M –  $1.8 \times 10^{-3}$  M) at a **Py-R** concentration of 10  $\mu\text{M}$  in DCM solvent under an argon atmosphere using Shimadzu fluorometer (RF-6000). In order to induce fluorescence quenching by *o*-NA, excitation was performed at  $\lambda_{\text{ex}} = 310$  nm, and their corresponding emission wavelength was monitored from  $\lambda_{\text{em}} = 441$ –536 nm (from **Py-CN** to **Py-OMe**). For *o*-NA sensor response was defined as  $I_0/I - 1$ . Stern-Volmer constants ( $K_{\text{sv}}$ ) ( $\text{M}^{-1}$ ) were calculated by Stern-Volmer equation,  $(I_0/I) = 1 + K_{\text{sv}} [Q]$ , where  $[Q]$  is the molar concentration of *o*-NA. The limit of detection (LOD) was calculated as follows: limit of detection equation =  $3\sigma/K$ . Where  $\sigma$  is the standard deviation and  $K$  is the slope between fluorescence versus *o*-NA concentration. The linear equation obtained from Stern-Volmer plot is  $y = 0.00345x - 0.31462$  ( $R = 0.992$ ).

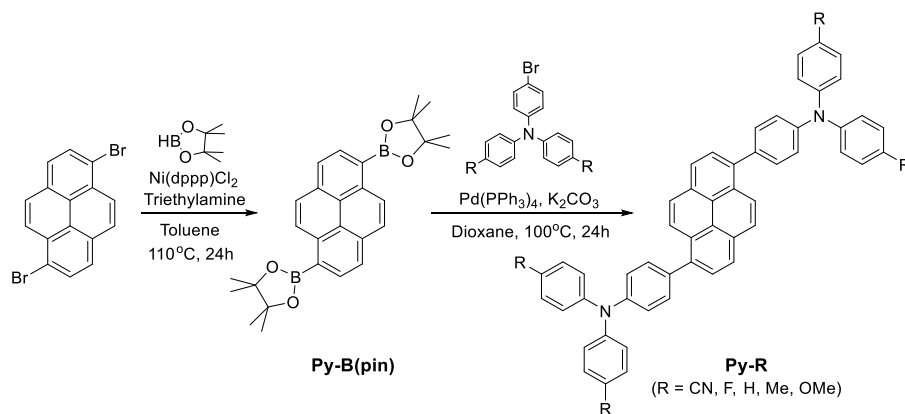
## 3. Results and discussion

### 3.1. Synthesis of **Py-R** compounds

**Scheme 1** shows the synthetic procedure used to produce a series of pyrene based D-A-D compounds, 1,6-bis[(*N,N*-*p*-(*R*)-diphenylamino)phenyl]pyrene (**R** = CN (**Py-CN**), F (**Py-F**), H (**Py-H**), Me (**Py-Me**), and OMe (**Py-OMe**)). Initially, the precursor for the acceptor unit 1,6-bis(4,4,5,5-tetramethyl-1,3,2-dioxaborolan-2-yl)pyrene (**Py-B(pin)**) and the precursor for donor units with various electron-donating (EDGs) or withdrawing groups (EWGs) at the *para*-positions of triphenylamine (TPA), 4-bromo-*N,N*-bis(*p*-(*R*)-phenyl)aniline, were prepared according as previously reported [35,36]. As shown in **Scheme 1**, **Py-B(pin)** was synthesized by a Ni(dppp)Cl<sub>2</sub> catalytic coupling reaction of 1,6-dibromopyrene and 4,4,5,5-tetramethyl-1,3,2-dioxaborolane. Then, the pyrene based D-A-D compounds were successfully synthesized using the modified Suzuki-Miyaura cross-coupling reaction using **Py-B(pin)** and 2 molar ratios of 4-bromo-*N,N*-bis(*p*-(*R*)-phenyl)aniline. The **Py-R** compounds were purified by silica gel column chromatography using *n*-hexane/dichloromethane (DCM) mixtures as eluents and further purified by recrystallization. The molecular structures of all compounds were characterized by  $^1\text{H}$  and  $^{13}\text{C}\{^1\text{H}\}$  NMR and elemental analysis. Detailed synthetic procedures and characterization data are provided in the Experimental Section and Supplementary data.

### 3.2. Photophysical properties

As shown in **Fig. 1**, steady-state UV–visible absorption and fluorescence spectra were measured both in solution and film states. Spectral parameters are summarized in **Table 1**. UV–vis absorption spectra showed structured and relatively intense absorption bands in the range 260–325 nm, which were attributed to  $\pi$ – $\pi^*$  transitions of substituted triphenylamine (TPA) and pyrene core (**Fig. S4**). Broad relatively weak absorption bands in the range 350–450 nm were attributed to intramolecular charge transfer (ICT) in the ground state from TPA (donor) to pyrene (acceptor). In addition, since TPA was located at the 1,6-positions of the active sites of pyrene with notable  $\pi$ -conjugation effect, it was confirmed that charge transfer occurs more readily in the ground state [38,39]. We compared the absorption wavelength bands of the **Py-R** compounds, to understand substituent effects. It was found that the low-energy band is relatively more affected than the high-energy band by the *para*-substituted TPA. In this context, comparisons of the absorption wavelength maxima of charge transfer bands showed absorption peak changes depended on substituents. On moving from electron-withdrawing groups (EWGs) to electron-donating groups (EDGs), absorption peaks were red-shifted in the following order  $\text{CN} < \text{F} < \text{H} < \text{Me} < \text{OMe}$ . Steady-state absorption spectral comparisons between **Py-CN** and the other compounds revealed **Py-CN** had a unique spectrum, due to the strong electron-withdrawing substituent character of the CN group. This phenomenon is further addressed in the DFT



Scheme 1. Synthesis of 1,6-bis[(*N,N*-*p*-(*R*)-diphenylamino)phenyl]pyrene (**Py-R**).

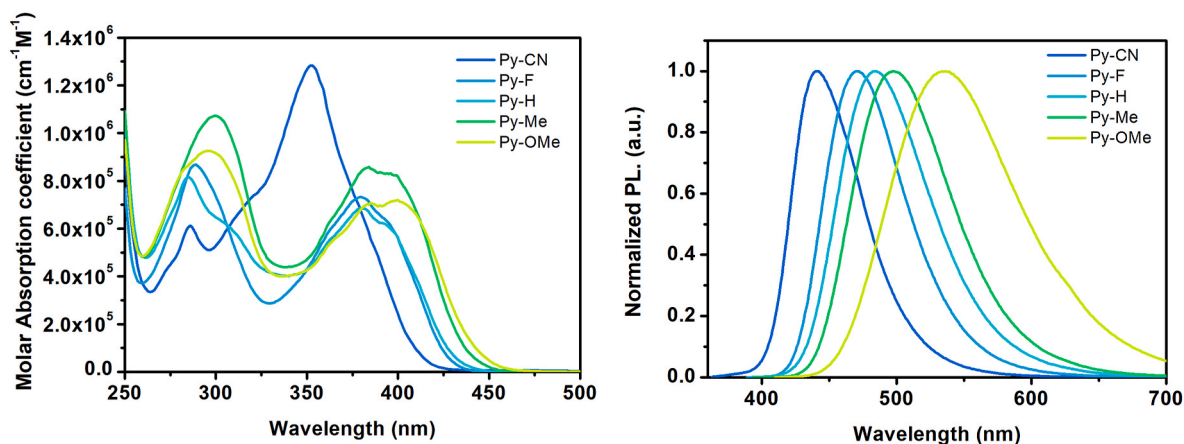


Fig. 1. UV-vis absorption (left) and emission (right) spectra of **Py-R** in DCM solution at a concentration of 10  $\mu\text{M}$ .

Table 1  
Photophysical properties of **Py-R**.

Compd	$\lambda_{\text{max}}^{\text{abs}}$ (nm) sol <sup>a</sup> /film <sup>b</sup>	$\lambda_{\text{max}}^{\text{PL}}$ (nm) sol <sup>a</sup> /film <sup>b</sup>	Stokes Shift ( $\text{cm}^{-1}$ )	$\Phi_f^c$ sol <sup>a</sup>	$\tau_f^d$ (ns)	$k_f^e \times 10^8$ ( $\text{s}^{-1}$ )	$k_{\text{nr}}^e \times 10^8$ ( $\text{s}^{-1}$ )	$k_f/k_{\text{nr}}$
Py-CN	353/358	441/480	5653	0.75	1.28	5.86	1.95	3.00
Py-F	379/387	471/495	5154	0.64	2.07	3.09	1.74	1.77
Py-H	379/414	483/482	5682	0.65	1.98	3.28	1.77	1.85
Py-Me	384/406	497/471	5921	0.65	2.05	3.17	1.71	1.85
Py-OMe	400/412	536/485	6344	0.50	2.16	2.31	2.31	1.00

<sup>a</sup> Measured in DCM at a concentration of 10  $\mu\text{M}$  at room temperature (RT).

<sup>b</sup> Measured in thin films.

<sup>c</sup> Relative to 9,10-diphenylanthracene ( $\Phi_{\text{PL}} = 0.95$ , ethanol) as standards, in DCM at RT.

<sup>d</sup> Fluorescence lifetimes in DCM.

<sup>e</sup> Values of  $k_f$  and  $k_{\text{nr}}$  were calculated using the equations,  $k_f = \Phi_f/\tau_f$  and  $k_{\text{nr}} = (1/\tau_f) - k_f$ .

calculation section below. To understand the intermolecular interactions in the steady-state absorption properties, the absorption spectra in the thin films were also shown in Fig. S7, and all of the compounds were found to exhibit a broad red-shift trend in comparison with their corresponding absorption spectra in solution, which implies that **Py-R** compounds may aggregate in a head-to-tail arrangement to form J-aggregates [40].

As shown in Fig. 1 (right), the emission maxima of **Py-R** ranged from 441 to 536 nm in dichloromethane (DCM) solution and their emission profiles ranged from blue to yellow. In the excited state, for **Py-R** emission spectra, the red-shift moving from EWGs to EDGs affects the emission color tuning. As was observed in their absorption spectra, the

emission maxima wavelengths were shifted according to the substituent effect in the fluorescence emission spectrum. In addition, we measured the solvent-dependent emission spectra for each **Py-R** compounds to determine the origins of emissions. Fig. S9 show that all compounds were red-shifted on increasing solvent polarity from *n*-hexane to acetonitrile (ACN), which indicated the presence of intramolecular charge transfer in the excited state. Furthermore, **Py-R** compounds showed more remarkable ICT characteristics on increasing the electron-donating power of substituents, which demonstrated charge transfer of **Py-R** compounds could be finely controlled using substituent effects.

In Table 1, fluorescence quantum yields ( $\Phi_f$ ) and fluorescence lifetimes ( $\tau_f$ ) were measured to explore excited state properties. Based on

measured fluorescence lifetimes, all emission decay profiles were well fitted by single exponential functions, suggesting radiative decay from a single specific excited state in Fig. S8. Radiative and non-radiative decay rate constants were calculated using the relationship between the  $\Phi_f$  and  $\tau_f$  values. To check the tendency according to the substituents, representatively, we compared **Py-CN** (an EWG) and **Py-OMe** (an EDG). **Py-CN** had relatively high  $\Phi_f$  and low  $\tau_f$  values, whereas **Py-OMe** had low  $\Phi_f$  and high  $\tau_f$  values. **Py-OMe** stabilized the D-A-D molecule more than the other compounds in the excited state, because of its electron-rich substituent character, which also resulted in a longer fluorescence lifetime. In addition, since **Py-OMe** had a bulky structure than the other compounds, more reorganization energy was required to return to the ground state structure, which affected fluorescence quantum yield. Consequently, these properties are determined from the molecular behavior induced by substituents in the excited state. As shown in Table 1, there was a general increasing trend in the  $k_r$  value as the electron withdrawing power increases but not in the  $k_{nr}$  value. This means that the  $k_r$  value is controlled by the electron-donating or withdrawing effects of substituents, and as a result, the  $k_r$  value plays a key role in the control of emission color.

The intramolecular charge transfer (ICT) process was further evaluated using relationships between Stokes shifts in various solvents and the Lippert-Mataga equation. Therefore, sensitivity of the solvent polarity can be analyzed in terms of the difference between the dipole moments in the ground ( $\mu_g$ ) and excited states ( $\mu_e$ ). Stokes shifts between the maximum absorption and emission wavelengths, in wavenumbers ( $\Delta\nu$ ), can be calculated using eq (1).

$$\Delta\nu = \bar{\nu}_a - \bar{\nu}_f = \frac{2}{hca_0^3} \left( \frac{\epsilon - 1}{2\epsilon + 1} + \frac{n^2 - 1}{2n^2 + 1} \right) \times (\mu_e - \mu_g)^2 + \text{constant}$$

$$= 2\Delta f \times \frac{(\Delta\mu)^2}{hca_0^3} + \text{constant} \quad (1)$$

Where  $\mu_e - \mu_g$  ( $\Delta\mu$ ) is the difference between the dipole moments of the excited and ground states,  $c$  is the speed of light,  $h$  is Planck's constant, and  $a_0$  is the radius of the Onsager cavity around the fluorophore. The dielectric constants ( $\epsilon$ ): ( $\epsilon$ : 1.88; *n*-hexane, 2.38; toluene, 7.6; tetrahydrofuran (THF), 9.1; DCM, 37.5; ACN) and the refractive indices ( $n$ ) of solvents are included in the term  $\Delta f$ , which is known as orientation polarizability. Onsager radii, which were obtained using B3LYP/6-31G, were considered to be half of the average size of 24.8, 23.5, 23.5, 25.1, and 26.3 Å for **Py-R** (R = CN, F, H, Me, and OMe, respectively).

Fig. 2 shows Lippert-Mataga plots for **Py-R** compounds in solvents

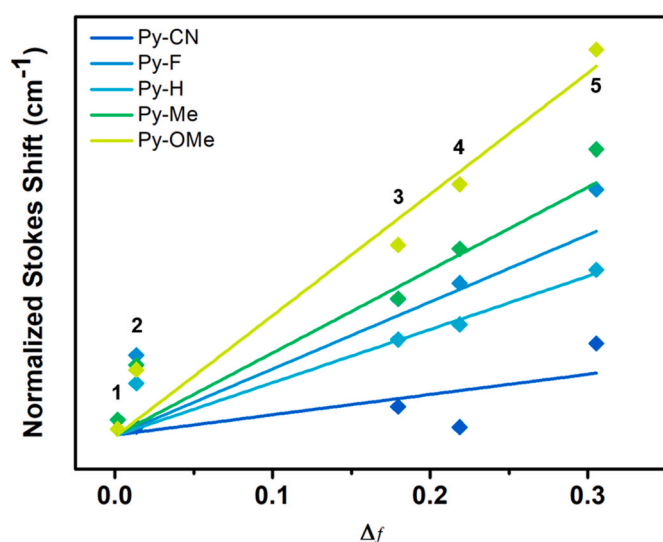


Fig. 2. Lippert-Mataga plots for **Py-R** compounds measured in various solvents (1: *n*-hexane, 2: toluene, 3: THF, 4: DCM, 5: ACN).

with different polarities. Using eq (1), values of dipole moment changes ( $\Delta\mu$ ) for **Py-R** were estimated to be 22.6, 37.8, 33.7, 46.5, and 60.3 Debye (D) for R = CN, F, H, Me, and OMe, respectively. Table S1 shows values of the ground state dipole moments ( $\mu_g$ ) for energy minimized structures obtained by the DFT method. Using ground state dipole moments ( $\mu_g$ ) and dipole moment changes ( $\Delta\mu$ ), the excited state dipole moments ( $\mu_e$ ) for **Py-R** were calculated to be 23.2, 37.9, 33.8, 46.7, and 60.4 D, respectively. This result explained that the excited state dipole moments of **Py-R** were positively correlated with charge transfer gaps in the excited state as measured by solvent-dependent emission spectroscopy (Fig. S9); greater electron-donating ability increased the charge transfer gap between *n*-hexane and ACN. In addition, as the electron-donating power increased, dipole moment changes ( $\Delta\mu$ ) also tended to increase (**Py-CN** < **Py-F**  $\approx$  **Py-H** < **Py-Me** < **Py-OMe**), which confirmed that this tendency was caused by substituent effects. Since the slope of the Lippert-Mataga plot and  $(\Delta\mu)^2$  are proportional, as shown by eq (1), this slope was also affected by substituents. Furthermore, the slope of the Lippert-Mataga plot quantitatively represents the ICT process in the excited state, indicating increases in slope are associated with large increases in charge transfer degree [41]. The tendency in slopes followed the order **Py-CN** < **Py-H** < **Py-F** < **Py-Me** < **Py-OMe**, which confirmed that charge transfer degree is dependent on the nature of substituents. Therefore, **Py-R** compounds indicate controllable ICT property in accordance with the substituent effect.

### 3.3. Electrochemical properties

As shown in Fig. 3, the electrochemical properties of **Py-R** were also investigated by cyclic voltammetry (CV), which was performed using a three-electrode cell system; a glassy carbon electrode was used as the working electrode, while a platinum wire and a saturated calomel electrode (SCE) were used as the counter and reference electrodes, respectively. All compounds showed reversible oxidation peaks, and first oxidation onset potentials of **Py-R** (R = CN, F, H, Me, and OMe) were located at 1.17, 0.84, 0.82, 0.73, and 0.64 V, respectively. Once a unit electron is taken out from the triarylamine to generate the oxidized form, the molecules are stabilized by the  $\pi$ -conjugation effect. Further, as the electron-donating group of the substituent is stronger, electron-rich conditions are formed, which stabilizes the molecule along with  $\pi$ -conjugation effect. These results also indicate values of the first oxidation onset potentials are affected by the substituent.

As shown in Table 2, experimental and calculated highest occupied molecular orbital (HOMO) and lowest unoccupied molecular orbital

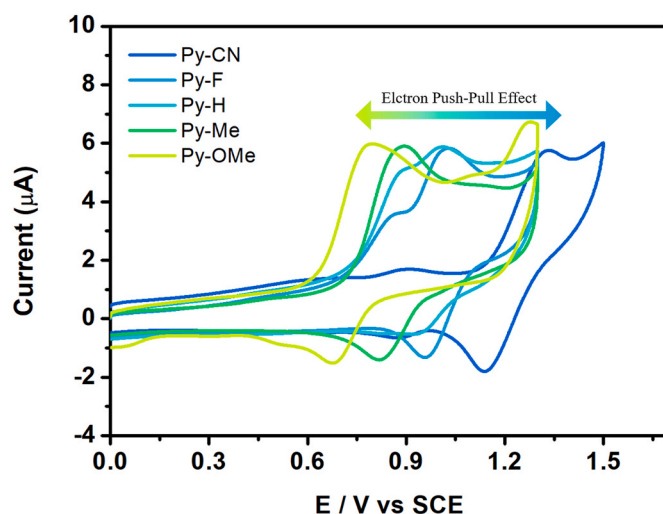


Fig. 3. Cyclic Voltammetry (CV) performed at a scan rate of 0.1 V s<sup>-1</sup> on **Py-R** compounds in DCM solution at a concentration of 100  $\mu$ M containing 0.1 M TBAP as electrolyte.

**Table 2**  
Energy band gap properties of **Py-R**.

Compounds	HOMO <sup>a</sup> (eV)	LUMO <sup>b</sup> (eV)	$E_g^{opt}$ (eV)	HOMO <sup>c</sup> (eV)	LUMO <sup>c</sup> (eV)	$E_g^c$ (eV)
<b>Py-CN</b>	-5.97	-2.97	3.00	-5.57	-2.18	3.39
<b>Py-F</b>	-5.64	-2.74	2.90	-4.92	-1.68	3.24
<b>Py-H</b>	-5.62	-2.76	2.86	-4.80	-1.58	3.22
<b>Py-Me</b>	-5.53	-2.69	2.84	-4.68	-1.51	3.17
<b>Py-OMe</b>	-5.44	-2.68	2.76	-4.51	-1.44	3.07

<sup>a</sup>  $E_{HOMO}(eV) = -e(E_{onset}^{ox} + 4.8)$ .

<sup>b</sup>  $E_{LUMO}(eV) = -e(E_{HOMO} + E_g^{opt})$ .

<sup>c</sup> Obtained by DFT calculation.

(LUMO) energy levels of the pyrene based D-A-D series were compared. Experimental HOMO energy levels were estimated from a first oxidation onset potential, indicating approximately  $-5.64 \pm 0.33$  eV. Because no cathodic reduction processes were measured, experimental LUMO energy levels were estimated using optical band gaps calculated from the edges of absorption spectra and HOMO energy levels. Most of LUMO energy levels show similar values compared to HOMO energy levels, indicating approximately  $-2.76 \pm 0.21$  eV. Calculated HOMO energy levels were in the range  $-4.92 \pm 0.65$  eV. Calculated LUMO energy levels were in the range  $-1.68 \pm 0.50$  eV, and all compounds had higher calculated HOMO and LUMO levels than experimental HOMO and LUMO levels. Experimental and calculated values of the HOMO and LUMO energy levels has been confirmed to be effectively adjusted according to electron-donating and withdrawing characteristics of substituents in pyrene based D-A-D series. Fig. 4 shows, experimental and calculated HOMO and LUMO energy levels of **Py-R** showed good linear correlations with  $\sigma_p$  values, showing that HOMO slopes are greater than LUMO slopes. On the basis of the correlation of HOMO/LUMO energy levels and Hammett substituent constants ( $\sigma_p$ ), we confirmed the impacts of substituents on HOMO levels and band gap tuning. Optical and calculated energy band gaps ( $E_g$ ) for **Py-R** are summarized in Table 2. When optical band gaps were compared on the **Py-H** basis, the difference of **Py-F** and **Py-CN** (0.04 and 0.14 eV, respectively) appeared according to the electron-withdrawing ability of substituents, and the difference of **Py-Me** and **Py-OMe** (0.02 and 0.1 eV, respectively) appeared according to the electron-donating ability of substituents. As the electron-withdrawing ability of the *para*-substituted TPA moiety increased, both energy band gaps gradually expanded, and which showed calculated energy gaps were larger than optical gaps. These results demonstrate that the band gap of the pyrene based D-A-D molecules can be significantly reduced, when compared with the pure pyrene molecule [42]. We suggest that only with effect of the substituents, emission properties of similar molecular structures are controlled systematically by tailoring energy band gaps.

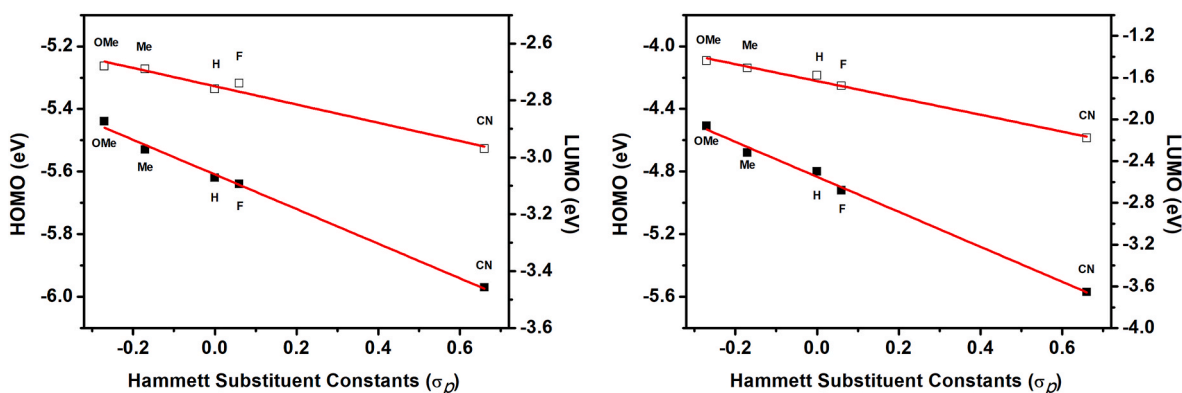


**Fig. 4.** Plots of experimental HOMO and LUMO energy levels versus Hammett substituent constants ( $\sigma_{para}$ ) (left) Plots of calculated HOMO and LUMO energy levels versus Hammett substituent constants ( $\sigma_{para}$ ) (right).

### 3.4. Theoretical studies

Fig. 5 and Fig. S11 shows HOMO and LUMO orbitals of pyrene based D-A-D compounds (**Py-R**), which were obtained by Gaussian 16 and visualized Chem3D and GaussView programs. Geometries were optimized by the DFT method using the B3LYP correlation function employing the 6-31G (d,p) level in the vacuum state. The H-1 orbitals of **Py-R** were delocalized on the TPA moiety, only. Whereas, for the HOMO orbitals, a gradual substituent-dependent changes in electron density were observed. As the electron-withdrawing power of substituents increased, electron density shifted strongly towards the pyrene moiety, and conversely, as the electron-donating power of substituents increased, it gradually expanded towards the TPA moiety. As mentioned above, this interpretation supports the notion that HOMO energy levels are dependent on substituent types, as shown in Fig. 4. The LUMO orbitals of **Py-R** compounds were almost delocalized on the pyrene moiety, and electron densities of L+1 orbitals shifted from pyrene to TPA as the electron-withdrawing power of substituents increased.

Fig. S12 and Table S3 shows the time-dependent DFT (TD-DFT) with the same functional and basis set confirm the origin of the  $\pi$ - $\pi^*$  transitions and the ICT transitions of **Py-R** with the spectral shift showing. TD-DFT calculations exhibited strong two distinct absorption bands that did not well match experimental data due to strong spectral shift of the ICT transition. In particular, the calculated absorption spectrum of TD-DFT allowed us to guess at the origin of the absorption spectrum of **Py-CN**. Considering the transition assignment of the spectra band, the ICT band of **Py-CN** was attributed of a major transition from HOMO to LUMO and a minor transition from H-1 to L+1 or L+2. The former corresponded to a transition from the pyrene moiety extended to phenyl containing a nitrogen atom as an electron donor to the pyrene core as an electron acceptor, whereas the latter corresponded to a transition from the TPA moiety, including its substituent, as an electron donor to the diphenyl moiety, including its substituent, as an electron acceptor. As a result, these two distinct types of electronic transitions by  $\pi$ - $\pi^*$  transition and ICT might explain the origin of the steady-state broad charge transfer band (experimental value 300–400 nm). In the case of the other compounds, ICT bands were attributed to major transitions from HOMO to LUMO and minor transitions from H-1 to LUMO. Major and minor transitions corresponded from the uniformly distributed D-A-D molecule and intensively distributed TPA moiety as an electron donor to the pyrene core as an electron acceptor. Through the calculation results, the main transition that affects the absorption spectra of pyrene based D-A-D compounds (**Py-R**) is due to intramolecular charge transfer and the calculation results support the experimental data. Therefore, we propose the energy band gap adjustment was due to the substituent-dependent ICT effect.

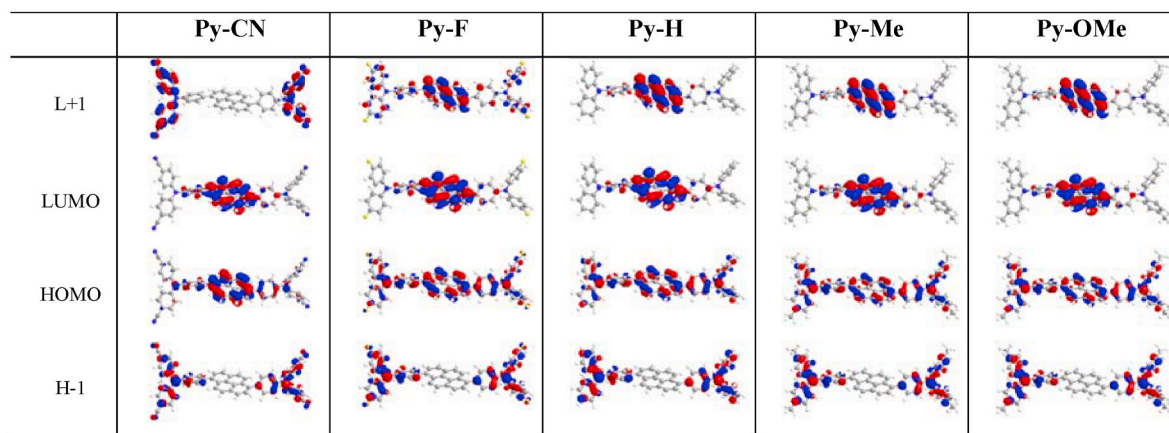


Fig. 5. Frontier orbital distributions (HOMO-1, HOMO, LUMO, LUMO+1) of **Py-R** calculated by DFT with the B3LYP function and 6-31G (d,p) basis.

### 3.5. Chemosensor

Efficient substituent-dependent energy band gap adjustment is expected to be applied to chemosensors. In general, higher spectral overlap between the absorbance band of an analyte and the emission band of luminescence material increases the probability of fluorescence resonance energy transfer (FRET) and hence fluorescence quenching [43]. The quenching phenomenon is applied to the detection of various analytes [44], and in the present study, *o*-NA was introduced as an analyte to detect nitro aromatic compounds used as explosives.

The sensitivities of **Py-R** to *o*-NA was estimated using Stern-Volmer constants,  $K_{sv}$ , determined using eq (2).

$$\frac{I_0}{I} = 1 + K_{sv}[Q] \quad (2)$$

where  $I_0$  and  $I$  are fluorescence intensities in the absence and presence of *o*-NA, respectively. Stern-Volmer plots were plotted as a function of *o*-NA concentration,  $[Q]$ . Stern-Volmer constants,  $K_{sv}$ , were calculated from slopes of Stern-Volmer plots. To observe emission quenching of **Py-R** by *o*-NA, we carried out fluorescence emission measurements in DCM. To prevent excessive quenching by *o*-NA, excitation was performed at 310 nm, at which *o*-NA absorption was relatively low. **Py-R** compounds ( $R = \text{CN, F, H, Me, and OMe}$ ) showed their emission wavelengths at 441, 471, 484, 497, and 536 nm, respectively, which confirmed spectral overlap between the absorption of *o*-NA and the emission of **Py-R** (Fig. 6 and Fig. S10). The degree of spectral overlap followed the order **Py-CN**

> **Py-F** > **Py-H** > **Py-Me** > **Py-OMe**, and the overlap increased with electron-withdrawing ability. This suggested that emission quenching by *o*-NA is more advantageous as the emission region of the **Py-R** compounds are blue-shifted. When the amount of *o*-NA was increased (from 0 to 180 equivalents), **Py-R** emissions were gradually quenched (Fig. S10), which indicated that **Py-R** compounds could be used to detect nitro explosives. The observed emission quenching can be attributed to the FRET from the photo-excited state of **Py-R** (electron donor) to the ground state of *o*-NA (electron acceptor) [34]. To quantify the degree of fluorescence quenching of **Py-R** compounds by *o*-NA, Stern-Volmer constants ( $K_{sv}$ ) were compared. The Stern-Volmer plots of **Py-R** ( $R = \text{CN, F, H, Me, and OMe}$ ) provided Stern-Volmer constants of 3171, 2164, 2276, 2083, and 2287  $\text{M}^{-1}$ , respectively (Fig. 7). **Py-CN** showed highest fluorescence quenching efficiency as shown in Figs. 6 and 7, and the other compounds showed similar degree of quenching. In addition, the limit of detection (LOD) of *o*-NA by **Py-CN** was determined by the limit of detection equation ( $3 \times \text{standard deviation/slope} = (3 \times 0.1601)/0.00345 [\mu\text{M}]$ ) and found to be 139  $\mu\text{M}$ . (Fig. 7) As shown in Table 1 and Fig. S6, the fluorescence emission of the **Py-OMe** has a lower  $k_r/k_{nr}$  value (1.00) and a higher  $k_{nr}$  value (2.31) than other **Py-R** compounds, which means that the activation of non-radiative processes has a remarkable effect on fluorescence quenching. These results indicated that fluorescence quenching of **Py-OMe**, as shown in Fig. S10, included a relatively dominant non-radiative effect of pure **Py-OMe** among the **Py-R** series as well as FRET for *o*-NA. On this basis, we found that

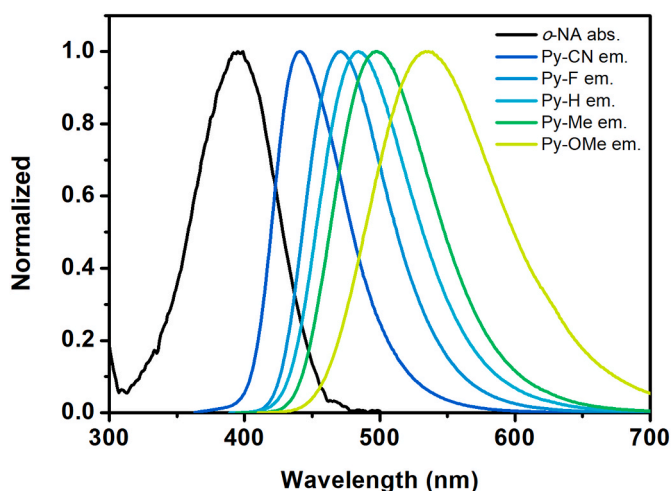


Fig. 6. Normalized absorption spectrum of *o*-NA and emission spectra of **Py-R** in DCM at a concentration of 10  $\mu\text{M}$ .

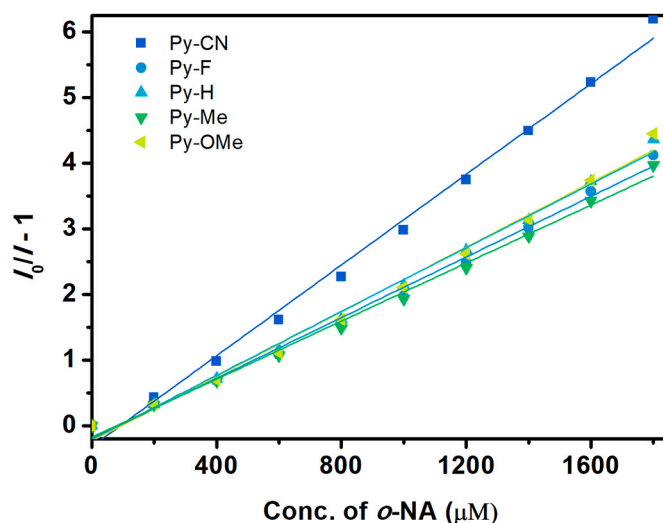


Fig. 7. Stern-Volmer plots for fluorescence quenching of **Py-R** in DCM at a concentration of 10  $\mu\text{M}$  when excited at 310 nm.

**Py-OMe** has the lowest fluorescence quenching efficiency by *o*-NA, despite having similar Stern-Volmer constants to **Py-F**, **H**, **Me**. Considering the specificity of **Py-OMe**, it is confirmed that effective energy transfer has occurred in the order **Py-CN** > **Py-F**, **H**, **Me** > **Py-OMe**. Thus, it was found that Stern-Volmer constants were also regulated by the substituent effect, which confirmed that spectral overlap and Stern-Volmer constants of **Py-R** compounds were positively correlated. Representatively, **Py-CN** showed more effective *o*-NA sensing potential than **Py-OMe**, as evidenced by large overlap between **Py-CN** emission and *o*-NA absorption, which confirmed that the efficient fluorescence emission quenching is controlled according to systematic energy band gaps by the various substituents. Based on these results, it is predicted that **Py-OMe** with a relatively longer wavelength of emission spectrum will show remarkable sensing efficiency for analytes with longer wavelength of absorption spectra, and such studies through energy band gap control are under investigation.

#### 4. Conclusions

Pyrene based D-A-D compounds, **Py-R** were synthesized using the Suzuki-Miyaura cross-coupling reaction. All of the compounds were characterized by several spectroscopic methods and their photophysical and electrochemical properties were studied. Especially, absorption spectra and Lippert-Mataga plots showed the nature of TPA derivatives attached to pyrene core significantly influenced ICT character in ground and excited states. Moreover, substituents enabled control of the ICT process and emission color adjustment from blue to yellow, and this was confirmed by correlation found between experimentally determined energy band gaps and Hammett constant ( $\sigma_{para}$ ). In particular, the **Py-R** compounds systematically regulates HOMO energy levels by the substituent. Theoretically calculated data by DFT and TD-DFT calculations provided a basis for experimental data by showing energy band gap regulation by the ICT effect in **Py-R**. Finally, **Py-R** compounds were used as selective chemosensors using the energy band gap control characteristic, and we observed fluorescence quenching with FRET mechanism by *o*-NA and especially **Py-CN** showed a high Stern-Volmer constant ( $3171 \text{ M}^{-1}$ ), which demonstrated the potential for the detection of nitro aromatic explosives. Further research is underway on fluorescence quenching by analytes that absorb at different wavelengths.

#### CRedit authorship contribution statement

**So-Yeon Kim**: Software, Formal analysis, Investigation, Writing – original draft, Visualization. **Min-Ji Kim**: Methodology, Data curation, Writing – review & editing. **Mina Ahn**: Methodology, Data curation, Writing – review & editing. **Kyeong-Min Lee**: Formal analysis, Investigation, Visualization. **Kyung-Ryang Wee**: Conceptualization, Writing – original draft, Supervision, Project administration, Funding acquisition.

#### Declaration of competing interest

The authors declare that they have no known competing financial interests or personal relationships that could have appeared to influence the work reported in this paper.

#### Acknowledgments

This research was supported by the Daegu University research grant. (20160393) The authors thank the Core Research Center for Natural Products and Medical Materials (CRCNM, supporting by Korea Basic Science Institute: National Research Facilities and Equipment Center) for technical support.

#### Appendix A. Supplementary data

Supplementary data to this article can be found online at <https://doi.org/10.1016/j.dyepig.2021.109362>.

#### References

- [1] Ledwon P, Motyka R, Ivaniuk K, Piduzhna A, Martyniuk N, Stakhira P, et al. The effect of molecular structure on the properties of quinoxaline-based molecules for OLED applications. *Dyes Pigments* 2020;173:108008. <https://doi.org/10.1016/j.dyepig.2019.108008>.
- [2] Reddy MR, Han SH, Lee JY, Seo S. Synthesis and characterization of quinoxaline derivative for high performance phosphorescent organic light-emitting diodes. *Dyes Pigments* 2018;153:132–6. <https://doi.org/10.1016/j.dyepig.2018.02.020>.
- [3] Chang DW, Ko S-J, Kim JY, Dai L, Baek J-B. Multifunctional quinoxaline containing small molecules with multiple electron-donating moieties: solvatochromic and optoelectronic properties. *Synth Met* 2012;162(13–14):1169–76. <https://doi.org/10.1016/j.synthmet.2012.04.016>.
- [4] Han P, Gong X, Lin B, Jia Z, Ye S, Sun Y, et al. Solution processable low bandgap thienoisindigo-based small molecules for organic electronic devices. *RSC Adv* 2015;5(62):50098–104. <https://doi.org/10.1039/C5RA07889J>.
- [5] Mei J, Diao Y, Appleton AL, Fang L, Bao Z. Integrated materials design of organic semiconductors for field-effect transistors. *J Am Chem Soc* 2013;135(18):6724–46. <https://doi.org/10.1021/ja400881n>.
- [6] Hasselman GM, Watson DF, Stromberg JR, Bocian DF, Holten D, Lindsey JS, et al. Theoretical solar-to-electrical energy-conversion efficiencies of Perylene–Porphyrin light-harvesting arrays. *J Phys Chem B* 2006;110(50):25430–40. <https://doi.org/10.1021/jp064547x>.
- [7] Chen Y, Zhu Y, Yang D, Zhao S, Zhang L, Yang L, et al. An azulene-containing low bandgap small molecule for organic photovoltaics with high open-circuit voltage. *Chem Eur J* 2016;22(41):14527–30. <https://doi.org/10.1002/chem.201603399>.
- [8] Mishra A, Bäuerle P. Small molecule organic semiconductors on the move: promises for future solar energy technology. *Angew Chem Int Ed* 2012;51(9):2020–67. <https://doi.org/10.1002/anie.201102326>.
- [9] Ahn M, Kim M-J, Cho DW, Wee K-R. Electron push–pull effects on intramolecular charge transfer in perylene-based donor–acceptor compounds. *J Org Chem* 2021;86(1):403–13. <https://doi.org/10.1021/acs.joc.0c02149>.
- [10] Wang C-Z, Ichihyanagi H, Sakaguchi K, Feng X, Elsegood MR, Redshaw C, et al. Pyrene-based approach to tune emission color from blue to yellow. *J Org Chem* 2017;82(14):7176–82. <https://doi.org/10.1021/acs.joc.7b00685>.
- [11] Wei J, Li Y, Song P, Yang Y, Ma F. Enhancement of one- and two-photon absorption and visualization of intramolecular charge transfer of pyrenyl-contained derivatives. *Spectrochim Acta A* 2021;245:118897. <https://doi.org/10.1016/j.saa.2020.118897>.
- [12] Liu L, Yang G, Duan Y, Geng Y, Wu Y, Su Z. The relationship between intermolecular interactions and charge transport properties of trifluoromethylated polycyclic aromatic hydrocarbons. *Org Electron* 2014;15(9):1896–905. <https://doi.org/10.1016/j.orgel.2014.05.020>.
- [13] Kim M-J, Ahn M, Shim JH, Wee K-R. Terphenyl backbone-based donor– $\pi$ -acceptor dyads: geometric isomer effects on intramolecular charge transfer. *Phys Chem Chem Phys* 2020;22(6):3370–8. <https://doi.org/10.1039/C9CP06466D>.
- [14] Hwang J, Ahn M, Choi J, Wee KR. Inter-ligand energy transfer process in an Ir-complex with expanding  $\pi$ -conjugated ligand. *ChemPhysChem* 2020;21(20):2320–6. <https://doi.org/10.1002/cphc.202000565>.
- [15] Ahn M, Kim M-J, Wee K-R. Electron push–pull effects in 3, 9-bis (p-(R)-diphenylamino) perylene and constraint on emission color tuning. *J Org Chem* 2019;84(18):12050–7. <https://doi.org/10.1021/acs.joc.9b01849>.
- [16] Wee K-R, Han W-S, Kim J-E, Kim A-L, Kwon S, Kang SO. Asymmetric anthracene-based blue host materials: synthesis and electroluminescence properties of 9-(2-naphthyl)-10-arylanthracenes. *J Mater Chem* 2011;21(4):1115–23. <https://doi.org/10.1039/C0JM02877K>.
- [17] Wang S, Cheng Z, Song X, Yan X, Ye K, Liu Y, et al. Highly efficient long-wavelength thermally activated delayed fluorescence OLEDs based on dicyanopyrazino phenanthrene derivatives. *ACS Appl Mater Interfaces* 2017;9(11):9892–901. <https://doi.org/10.1021/acsami.6b14796>.
- [18] Odom SA, Parkin SR, Anthony JE. Tetracene derivatives as potential red emitters for organic LEDs. *Org Lett* 2003;5(23):4245–8. <https://doi.org/10.1021/ol035415e>.
- [19] Islam MM, Hu Z, Wang Q, Redshaw C, Feng X. Pyrene-based aggregation-induced emission luminogens and their applications. *Mater. Chem. Front.* 2019;3(5):762–81. <https://doi.org/10.1039/C9QM00090A>.
- [20] Wee K-R, Ahn H-C, Son H-J, Han W-S, Kim J-E, Cho DW, et al. Emission color tuning and deep blue dopant materials based on 1, 6-bis (N-phenyl-p-(R)-phenylamino) pyrene. *J Org Chem* 2009;74(21):8472–5. <https://doi.org/10.1021/jo901783a>.
- [21] Mohr A, Talbiersky P, Korth H-G, Sustmann R, Boese R, Bläser D, et al. A new pyrene-based fluorescent probe for the determination of critical micelle concentrations. *J Phys Chem B* 2007;111(45):12985–92. <https://doi.org/10.1021/jp0731497>.
- [22] Focsaneanu K-S, Scaiano J. Potential analytical applications of differential fluorescence quenching: pyrene monomer and excimer emissions as sensors for electron deficient molecules. *Photochem Photobiol Sci* 2005;4(10):817–21. <https://doi.org/10.1039/B505249A>.

- [23] Zhang S, Qiao X, Chen Y, Wang Y, Edkins RM, Liu Z, et al. Synthesis, structure, and opto-electronic properties of regioisomeric pyrene-thienoacenes. *Org Lett* 2014;16(2):342–5. <https://doi.org/10.1021/ol402971n>.
- [24] Chopra R, Kaur P, Singh K. Pyrene-based chemosensor detects picric acid upto attogram level through aggregation enhanced excimer emission. *Anal Chim Acta* 2015;864:55–63. <https://doi.org/10.1016/j.aca.2015.01.029>.
- [25] Liang Z-Q, Li Y-X, Yang J-X, Ren Y, Tao X-T. Suppression of aggregation-induced fluorescence quenching in pyrene derivatives: photophysical properties and crystal structures. *Tetrahedron Lett* 2011;52(12):1329–33. <https://doi.org/10.1016/j.tetlet.2011.01.060>.
- [26] Xu J-Q, Liu W, Liu S-Y, Ling J, Mai J, Lu X, et al. ADA small molecule donors based on pyrene and diketopyrrolopyrrole for organic solar cells. *Sci China Chem* 2017;60(4):561–9. <https://doi.org/10.1007/s11426-016-9003-9>.
- [27] Wang C-Z, Pang Z-J, Yu Z-D, Zeng Z-X, Zhao W-X, Zhou Z-Y, et al. Short axially asymmetrically 1, 3-disubstituted pyrene-based color-tunable emitters: synthesis, characterization and optical properties. *Tetrahedron* 2021;78:131828. <https://doi.org/10.1016/j.tet.2020.131828>.
- [28] Kathiravan A, Srinivasan V, Khamrang T, Velusamy M, Jaccob M, Pavithra N, et al. Pyrene based D- $\pi$ -A architectures: synthesis, density functional theory, photophysics and electron transfer dynamics. *Phys Chem Chem Phys* 2017;19(4):3125–35. <https://doi.org/10.1039/C6CP08180K>.
- [29] Wang S-L, Ho T-I. Substituent effects on intramolecular charge-transfer behaviour of styrylheterocycles. *J Photochem Photobiol A* 2000;135(2–3):119–26. [https://doi.org/10.1016/S1010-6030\(00\)00289-6](https://doi.org/10.1016/S1010-6030(00)00289-6).
- [30] Liu Q, Yu S, Zhao Z, Zhang X, Liu R. Three anthracene-based bis-imidazolium salts: synthesis, structure and recognition for 2, 4-dinitrophenylhydrazine. *Dyes Pigments* 2020;173:107983. <https://doi.org/10.1016/j.dyepig.2019.107983>.
- [31] Fang Q, Geng J, Liu B, Gao D, Li F, Wang Z, et al. Inverted opal fluorescent film chemosensor for the detection of explosive nitroaromatic vapors through fluorescence resonance energy transfer. *Chem Eur J* 2009;15(43):11507–14. <https://doi.org/10.1002/chem.200901488>.
- [32] Bagheri M, Masoomi MY, Morsali A. Highly sensitive and selective ratiometric fluorescent metal-organic framework sensor to nitroaniline in presence of nitroaromatic compounds and VOCs. *Sensor Actuator B Chem* 2017;243:353–60. <https://doi.org/10.1016/j.snb.2016.11.144>.
- [33] Bhalla V, Arora H, Singh H, Kumar M. Triphenylene derivatives: chemosensors for sensitive detection of nitroaromatic explosives. *Dalton Trans* 2013;42(4):969–74. <https://doi.org/10.1039/C2DT31459B>.
- [34] Lee J, Park Y, Jung J, Han W-S. Blue-shifted aggregation-induced emission of siloles by simple structural modification and their application as nitro explosive chemosensors. *Photochem Photobiol Sci* 2017;16(10):1495–501. <https://doi.org/10.1039/C7PP00268H>.
- [35] Yang DS, Kim KH, Cho MJ, Jin JI, Choi DH. Donor-acceptor alternating  $\pi$ -conjugated polymers containing Di (thiophen-2-yl) pyrene and 2, 5-Bis (2-octyldodecyl) pyrrole [3, 4-c] pyrrole-1, 4 (2H, 5H)-dione for organic thin-film transistors. *J Polym Sci, Polym Chem Ed* 2013;51(6):1457–67. <https://doi.org/10.1002/pola.26518>.
- [36] Lumpi D, Holzer B, Binting J, Horkel E, Waid S, Wanzenböck HD, et al. Substituted triphenylamines as building blocks for star shaped organic electronic materials. *New J Chem* 2015;39(3):1840–51. <https://doi.org/10.1039/C4NJ01695E>.
- [37] Morris JV, Mahaney MA, Huber JR. Fluorescence quantum yield determinations. 9, 10-Diphenylanthracene as a reference standard in different solvents. *J Phys Chem* 1976;80(9):969–74. <https://doi.org/10.1021/j100550a010>.
- [38] Kurata R, Ito A, Gon M, Tanaka K, Chujo Y. Diarylamino-and diarylboryl-substituted donor-acceptor pyrene derivatives: influence of substitution pattern on their photophysical properties. *J Org Chem* 2017;82(10):5111–21. <https://doi.org/10.1021/acs.joc.7b00315>.
- [39] Feng X, Tomiyasu H, Hu J-Y, Wei X, Redshaw C, Elsegood MR, et al. Regioselective substitution at the 1, 3-and 6, 8-positions of pyrene for the construction of small dipolar molecules. *J Org Chem* 2015;80(21):10973–8. <https://doi.org/10.1021/acs.joc.5b02128>.
- [40] Würthner F, Kaiser TE, Saha-Möllner CR. J-aggregates: from serendipitous discovery to supramolecular engineering of functional dye materials. *Angew Chem Int Ed* 2011;50(15):3376–410. <https://doi.org/10.1002/anie.201002307>.
- [41] Sumalekshmy S, Gopidas K. Photoinduced intramolecular charge transfer in donor-acceptor substituted tetrahydropyrenes. *J Phys Chem B* 2004;108(12):3705–12. <https://doi.org/10.1021/jp022549l>.
- [42] Jang H-S, Cho H-S, Uhrig D, Nieh M-P. Insight into the interactions between pyrene and polystyrene for efficient quenching nitroaromatic explosives. *J Mater Chem C* 2017;5(47):12466–73. <https://doi.org/10.1039/C7TC04288D>.
- [43] Ji N-N, Shi Z-Q, Hu H-L, Zheng H-G. A triphenylamine-functionalized luminescent sensor for efficient p-nitroaniline detection. *Dalton Trans* 2018;47(21):7222–8. <https://doi.org/10.1039/C8DT01240G>.
- [44] Medintz IL, Clapp AR, Mattoussi H, Goldman ER, Fisher B, Mauro JM. Self-assembled nanoscale biosensors based on quantum dot FRET donors. *Nat Mater* 2003;2(9):630–8. <https://doi.org/10.1038/nmat961>.